Modulation of the Bifurcation in Radiative-Convective Equilibrium by Gray-Zone Cloud and Turbulence Parameterizations

Xiaoming Shi[1] and Yiyuan Fan[1]

[1]Division of Environment and Sustainability, Hong Kong University of Science and Technology, Hong Kong, China

Key Points:

- Convective self-aggregation in the radiative-convective equilibrium exhibits nonlinear dependence on cloud and turbulence parameterizations.
- Its emergence or suppression is governed by a bifurcation of the dynamical system, which is sensitive to subgrid processes in the gray zone.
- Bifurcation mechanisms might be barriers to climate predictability due to inherent uncertainties in cloud and turbulence parameterizations.

Corresponding author: Xiaoming Shi, shixm@ust.hk

Abstract

This study investigates the mechanisms by which small-scale turbulence and cloud physics determine the organization of large-scale convection in radiative-convective equilibrium (RCE), an idealization of the tropical atmosphere. Under uniform forcings similar to typical tropical conditions, the atmosphere in RCE might spontaneously separate into dry and moist regions on scales of 100-1000 km, with convective clouds aggregating into a cluster in the latter. This phenomenon is known as convective self-aggregation. Herein, we demonstrate that subtle changes in assumptions related to cloud physics and turbulence on scales of $\leq$1 km can dictate the emergence or suppression of convective self-aggregation, resulting from a bifurcation of the dynamical system. The bifurcation occurs when a small dry patch forms in the domain and is sustained because it contributes to negative effective diffusivity of the circulation. Cloud-radiation feedbacks and turbulence circulation interactions govern the formation of such dry patches, thereby modulating the bifurcation. This sensitive dependence on subgrid process models might be a fundamental barrier to climate predictability in light of inherent uncertainties in microscale processes. Because without the capability to include exact representations of those processes in climate models, slight differences in the different approximations used by modelers can lead to qualitative changes in climate predictions, at least for some processes.

Plain Language Summary

The tropical atmosphere may self-organize into well-separated moist and dry regions, with clustered clouds and rain in the former and clear-sky and dry air in the latter. This phenomenon is called convective self-aggregation and could dramatically impact tropical weather and climate by changing rainfall patterns and clouds distribution. However, we found that in an advanced cloud-resolving model, the atmosphere may either stay in a homogeneous state or exhibit self-aggregation, depending on how clouds and turbulence are represented. All physical models we chose are state-of-the-art physical models, yet the equilibrium state of the atmosphere is susceptible to subtle details of the cloud and turbulence models. This sensitivity to cloud and turbulence representations may pose another kind of "butterfly effect". Here, instead of facing uncertainties in initial conditions, what can potentially lead to qualitative, dramatic differences in predictions are the relatively small uncertainties in the physical models of cloud and turbulence. To the extent that our cloud and turbulence models can only be imperfect approximations and therefore have inherent uncertainties, the quest to reduce the disagreement between different climate models may eventually meet fundamental barriers.

1 Introduction

Thanks to the advances in computing power, modern numerical weather prediction (NWP) has achieved regional resolutions of ~1 km (Lean et al., 2008; Seity et al., 2011; Raynaud & Bouttier, 2017). Global simulations at kilometer-scale resolutions are also actively achieved by the modeling community (Wedi et al., 2020). However, grid spacings of such sizes also inhibit weather and climate models according to phenomena, such as turbulence in the gray zone (also known as terra incognita). The gray zone refers to situations in which the model mesh cannot fully resolve turbulence and in which turbulence cannot be assumed to be mostly unresolved and in a quasi-equilibrium state (Wyngaard, 2004; Chow et al., 2019). Since such assumptions form the basis of traditional turbulence models in large-eddy simulations (LES) and NWP models, both LES-type and NWP-type turbulence models may underperform in the gray zone.

Another challenge facing modern weather and climate models is the representation of microscale cloud physics (Morrison et al., 2020). Kilometer-scale grid spacings are far from sufficient to resolve cloud particles per se; however, they can partially resolve cloud cells, at least for deep convection. In such convection-permitting simulations (CPM), turbulent motions and cloud droplets are expected to exhibit more direct interactions; thus, cloud physics could have a significant impact on the simulated weather system (Morrison et al., 2011; Bryan & Morrison, 2012; Adams-Selin et al., 2013). For this reason, more sophisticated cloud physics schemes have been implemented in recent CPM systems (Benjamin et al., 2016; Milbrandt et al., 2016). Yet, due to uncertainties

in microphysical process rates, especially those of ice phase processes, further research into cloud microphysics is required (Morrison et al., 2020).

In this study, we investigate the dependence of convection organization in CPM simulations of radiative-convective equilibrium (RCE). RCE is a widely accepted idealization for the tropical atmosphere; indeed, its use can be traced back to an early single-column model study by Manabe and Strickler in 1964 (Manabe & Strickler, 1964). Modern RCE studies have used CPMs as a tool to evaluate an extensive list of tropical dynamics problems, such as the hydrological cycle (Romps, 2011), tropical cyclogenesis (Wing et al., 2016), atmospheric boundary layer (D. Yang, 2018), and others (Wing et al., 2018).

An interesting phenomenon in CPM simulations of RCE is that with uniform incoming solar radiation and sea surface temperature (SST) as boundary conditions, the simulation domain can sometimes exhibit a nonhomogeneous distribution of convective clouds. This process is referred to as convection self-aggregation, in which anomalously dry regions appear and convection spontaneously organizes into a single cluster (Bretherton et al., 2005). Self-aggregation in RCE is generally understood as the result of cloud-radiation interactions and surface enthalpy flux feedback (Bretherton et al., 2005; Emanuel et al., 2014; Beucler & Cronin, 2016). However, some authors have suggested that without radiation or surface enthalpy flux feedbacks, self-aggregation can still occur due to the effects of latent heating in the generation of available potential energy (D. Yang, 2019).

Here, we use RCE to explore the impact of turbulence models and cloud microphysics on the simulation of convection in the gray zone. Two state-of-the-art cloud microphysics schemes and two classic turbulence models are utilized in Cloud Model 1 (CM1) (Bryan & Fritsch, 2002) to conduct four experiments with a 2×2 factorial design. We find that there is no definite answer with regard to which microphysics or turbulence scheme favors convection self-aggregation. Instead, turbulence (microphysics) schemes can either support or suppress the development of self-aggregation, depending on with which microphysics (turbulence) scheme it is combined. We demonstrate that distinct behavior in simulations reflects a bifurcation of the underlying dynamical system. Homogeneous and clustered cloud distributions indicate different equilibrium states of the RCE, the latter of which forms and becomes accessible as the parameters of the dynamical system vary. Although cloud processes and turbulence are microscale phenomena, they modulate the macroscale parameters of the dynamical system of the atmosphere, thereby governing the probability of bifurcation.

2 Model and Methods

2.1 Experimental Design

Our numerical experiments used the Cloud Model 1 (CM1) (Bryan & Fritsch, 2002) Release 20.2. The simulation domain is $1080 \times 1080\,\mathrm{km}^2$ in the horizontal directions and 28 km in the vertical direction. The horizontal grid spacing is 3 km, and the vertical grid spacing ranges from 50 m near the surface to 500 m in the upper levels. The simulation has a uniform SST fixed at 301 K. Incoming solar radiation at the top of the atmosphere exhibits no diurnal cycle and is fixed at $650.83\,\mathrm{W\,m^{-2}}$, with a zenith angle of 50.5°. Numerical experiments were integrated for 100 days. A fifth-order scheme was adopted for computing horizontal and vertical advections. For the computation of scalar advection, the fifth-order weighted essentially nonoscillatory scheme was employed.

We adopted two PBL turbulence schemes and two cloud microphysics schemes to complete a total of four experiments. The microphysics schemes used were the Morrison (M) (Morrison et al., 2009) and Thompson (T) (Thompson et al., 2008) schemes. The former of which is a two-moment bulk microphysical approach that predict both the mass and number concentrations of cloud and precipitation species; and the latter has double-moment ice and rain. The PBL turbulence schemes include a Louis-type scheme (L) and an EDMF scheme (E). The former is a variant of the classic Smagorinsky scheme and considers only vertical mixing (Bryan & Rotunno, 2009); the latter was developed and adopted for operational weather forecast models (Hong & Pan, 1996). It can model counter-gradient (i.e., nonlocal) mixing and allows the vertical mass flux to penetrate the top of

the PBL and influence layers above the PBL. Combinations of these options yielded a total of four experiments: ML, TL, ME, and TE.

2.2 Mesoscale Blocks and Low-Pass Filter

We extensively used block averaging in our analysis to focus on mesoscale organization. Data from mesoscale blocks refer to the average results of horizontal partitioning of the simulation domain into 15×15 ($72 \times 72\,\mathrm{km}^2$) blocks and the horizontal averaging of data within each block. This procedure followed the analysis detailed in (Bretherton et al., 2005).

2.3 Frozen Moist Static Energy (MSE)

Frozen MSE is conserved during moist adiabatic processes and is used in this study to indicate the state of an atmosphere column. We simply refer it as MSE throughout the text. The MSE (h_f) is defined as follows,

$$h_f = c_p T + gZ + L_v q_v - L_f q_i, \tag{1}$$

where c_p denotes the specific heat of air at constant pressure, T is the temperature, g is the gravitational constant, Z is the geopotential height, L_v and L_f are the latent heat of vaporization and sublimation, respectively, and qv and qi are the specific ratios of water vapor and cloud ice, respectively. For conciseness, we refer frozen MSE as MSE throughout the article. The vertically integrated MSE is

$$H = \int \rho h_f \, dz, \tag{2}$$

and the budget equation of column MSE is

$$\frac{\partial H}{\partial t} = F_{SE} + R_{SW} + R_{LW} + A, \tag{3}$$

where F_{SE} denotes surface enthalpy flux, R_{SW} and R_{LW} are net heating to the column by shortwave and longwave radiations, respectively, and A is the advection term representing the net convergence of H due to circulation. Subtracting the horizontal mean from Equation (3) and multiplying the remaining equation by the deviation of column MSE yield the budget equation for column MSE variance as follows:

$$\frac{1}{2}\frac{\partial [H'^2]}{\partial t} = [H' F'_{SE}] + [H' R'_{SW}] + [H' R'_{LW}] + [H' A'], \tag{4}$$

where the prime indicates deviations from horizontal mean and the square brackets denote the horizontal average.

2.4 Linearization of Column MSE Equation

Here we derive a linearized column MSE budget equation, which is used for statbility analysis later. Following the approach detailed in Bretherton et al. (2005), the deviation of radiative forcing from the horizontal mean of RCE can be parameterized as a function of precipitation anomaly (P'), which represents the degree of cloudiness that dominates radiation perturbations,

$$R' = R'_{SW} + R'_{LW} = C_R L_v P', \tag{5}$$

where C_R denotes the strength of the cloud-radiation feedback. In Bretherton et al. (2005), the surface enthalpy flux anomaly was parameterized as a function of the precipitation anomaly as gustiness induces more surface evaporation. However, as will be shown in Fig. 3.1, evaporation in extremely dry regions can also be large due to the low relative humidity of the ambient air. Thus, we conceptually parameterize the surface enthalpy flux anomaly as a sum of two terms as follows:

$$F_{SE} = C_{S1} L_v P' + C_{S2} H_* r' \tag{6}$$

where H_* denotes the column MSE when an entire column is saturated, r' is the column relative humidity (CRH) anomaly, $H' = H_* r'$, and $CS1$ and $CS2$ are the sensitivity of surface enthalpy flux

to gustiness and relative humidity, respectively. The first term dominates in moist regions, whereas the second term dominates in dry regions. Subsequently, we seek an expression of P' in terms of r'. Because Bretherton et al. (2005) has demonstrated that precipitation in the RCE has an approximate exponential dependence on CRH, we can express precipitation as follows:

$$P = P_{\mathrm{RCE}} \exp(r') \tag{7}$$

where P_{RCE} denotes the mean precipitation in the RCE, enabling the precipitation anomaly to be approximated as follows:

$$P' = P_{\mathrm{RCE}}(e^{r'} - 1) \approx r' P_{\mathrm{RCE}}, \tag{8}$$

where r' is assumed to be small. Furthermore, we approximate the advection term by effective eddy diffusion as follows:

$$A' = \nu \nabla^2 H', \tag{9}$$

Combining Equations (3) and (5)–(9), we can express the linearized budget equation for H' as follows:

$$\frac{\partial H'}{\partial t} = (\beta_S + \beta_R) H' + \nu \nabla^2 H', \tag{10}$$

in which,

$$\beta_S = C_{S1} \frac{L P_{\mathrm{RCE}}}{H_*} + C_{S2}, \qquad \beta_R = C_R \frac{L P_{\mathrm{RCE}}}{H_*}, \tag{11}$$

are the strengths of surface enthalpy flux feedback and radiation feedback.

3 Results

3.1 Distinct Equilibrium States

Figure 1 presents the distribution of convection at the end of each of the four simulation, ML, TL, ME, and TE. In the TL and ME simulations, convection self-organizes into an elongated cluster. Relatively low outgoing longwave radiation (OLR) in the TL experiment suggests that the deep convection in TL is more intense and produces colder cloud tops compared with that in ME (Fig. 1F and G). Contrarily, ML and TE did not exhibit self-aggregation by day 100. The distributions of convection and clouds are highly homogeneous in ML. In TE, however, deep convection appears to be suppressed in some parts of the domain, whereas the overall distribution of convection is still random. We integrated ML and TE until day 150, finding that ML exhibits no sign of self-aggregation by this time, whereas TE exhibits partial self-aggregation.

As described in previous literature, convection self-aggregation features the formation of anomalously dry regions surrounding the convection cluster. This characteristic can be observed clearly in the distribution of vertically integrated frozen moist static energy (MSE) in Fig. 1E-H. The variability of MSE in a column is primarily controlled by the amount of moisture, i.e., the contours in Fig. 1F and H indicate sharp contrasts in water content between regions occupied by convection clusters and their surroundings. In ML, there is almost no column MSE gradient. In TE, a small dry patch (upper-right corner of Fig. 1H) was formed by day 100. This small dry patch enlarged in the continued simulation until it occupied approximately a quarter of the domain by day 150. Thus, the TE experiment is potentially capable of causing convection to self-organize into a single cluster; however, the growth of column MSE gradients is suppressed and slow.

As mentioned above, the most surprising aspect in those four experiments is the nonlinear dependence of convection organization on the representation of microscale processes. It is not possible to unambiguously demonstrate whether one turbulence (or microphysics) scheme favors convection self-aggregation while the other does not. In Section 4, we argue that these intriguing results depend on how macroscale characteristic parameters of the atmosphere are influenced by microscale processes, i.e., whether or not bifurcation occurs.

Another interesting result, as presented in Fig. 1A-D, is the dependence of surface evaporation on convection organization. In ML and TE, surface moisture flux is more intense below convection,

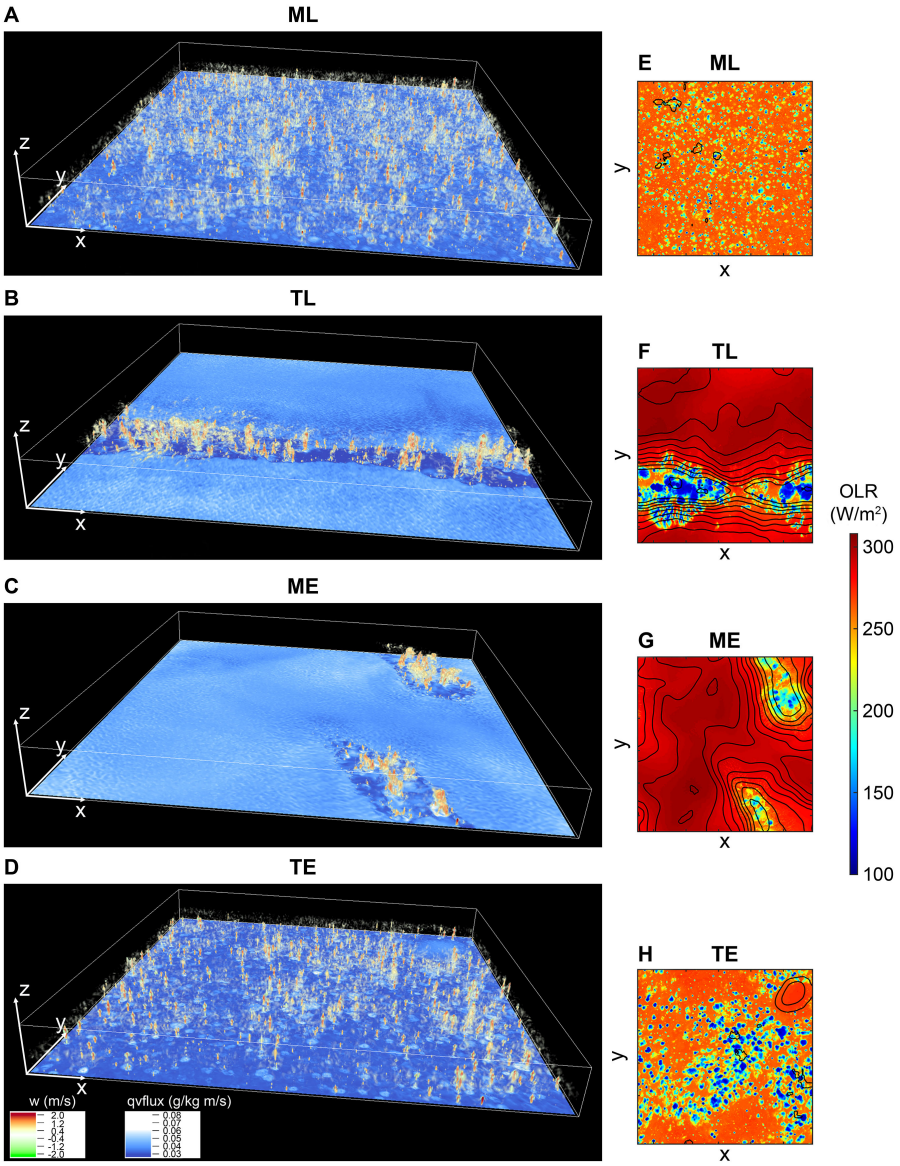

Figure 1. Distribution of convection at the end of the simulations. (**A-D**) Distribution of vertical velocity (w) (green to red color by volume rendering) and surface evaporation ("qvflux") (blue to white at the bottom of the domain) in the four experiments on day 100. (**E-H**) Distribution of outgoing longwave radiation (OLR) (color shading) and vertically integrated frozen moist static energy (MSE) (contours) in the four experiments on day 100. MSE contours are based on values from the mesoscale block and are given at intervals of $1 \times 10^7\,\mathrm{J\,m^{-2}}$.

which causes gustiness and enhances surface evaporation. However, in TL and ME, although the effect of gustiness still exists, the domain-scale variability of surface moisture flux is dominated by the construct between dry and wet regions. Due to their low atmospheric relative humidity, dry regions exhibit a much stronger surface evaporative flux than regions under deep convection.

3.2 Column MSE Variance Budget

The development of a horizontal gradient in column MSE enables us to quantify the process of convection self-aggregation with variance of column MSE (Fig. 2A). Simulations were initialized

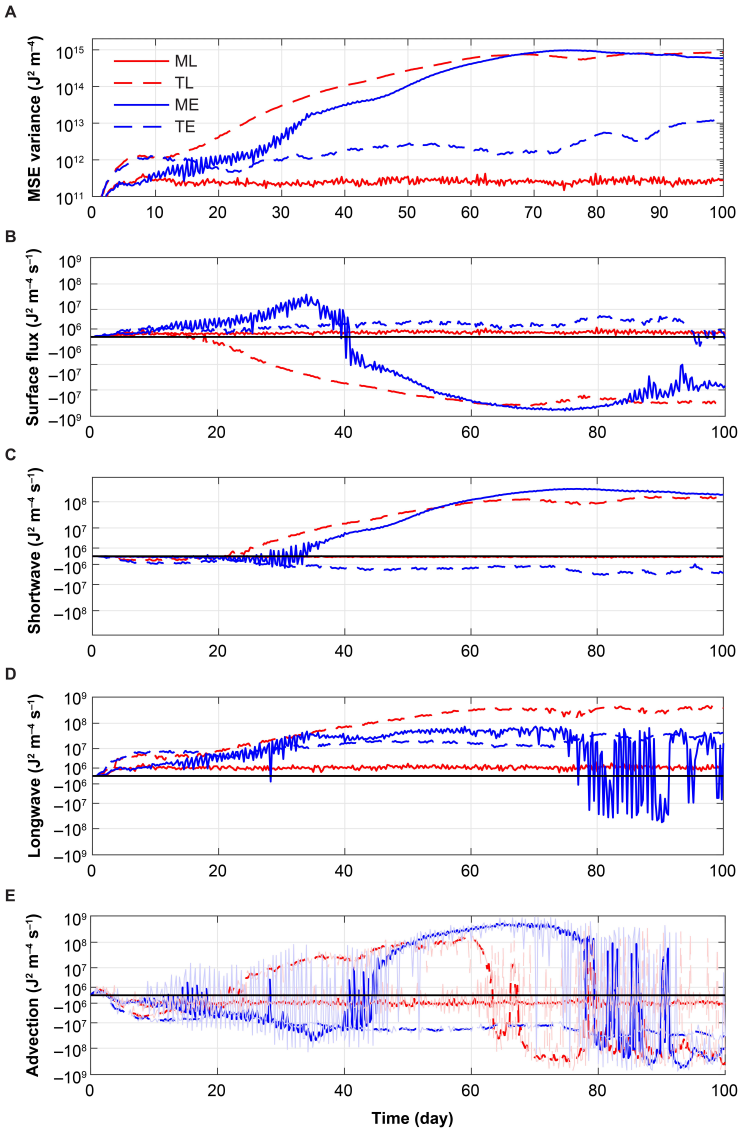

Figure 2. Variance of vertically integrated MSE (**A**) and its budget (**B-E**). The processes contributing to the tendency of the vertically integrated MSE include surface enthalpy flux (**B**), shortwave radiation (**C**), longwave radiation (**D**), and horizontal advection (**E**). The column MSE and budget terms are mesoscale block values. In (**E**), the semi-transparent curves denote 6-hourly data of the advection contribution, whereas the solid curves represent daily data with sub-daily variability filtered out.

from fields with very small amounts of random perturbations in potential temperature below 1 km. During the first 5 days, random deep convection bursts and column MSE variance increased from $10^6\,\mathrm{J^2m^{-4}}$ to 10^{11}–$10^{12}\,\mathrm{J^2m^{-4}}$. After this initial burst of convection, the self-aggregated simulations (TL and ME) exhibited continued growth of column MSE variance, reaching magnitudes of $10^{15}\,\mathrm{J^2m^{-4}}$, whereas the other two simulations exhibited very slow or no further growth.

Following Wing and Emanuel (2014), the time tendency of column MSE variance can be partitioned into contributions from four processes, namely, surface enthalpy flux, shortwave radiation, longwave radiation, and advection [Equation (4)]. Figure 2B–E presents the contributions of those processes.

Surface enthalpy flux contributions (Fig. 2B) are weakly positive for the ML and TE simulations, which have no significant self-aggregation, and mostly negative for the TL and ME runs. Notably, the ME simulation exhibits a significant positive surface flux contribution prior to day 40. The sign of the surface enthalpy flux contribution depends on whether the domain-scale variability of evaporation is dominated by gustiness or the relative humidity of the air. Gustiness exhibits a positive correlation with convection in space. Thus, it produces a positive contribution. Contrarily, relative humidity evaporation correlation is negative in space.

Radiation contributions (Fig. 2C and D) are mostly positive, with larger magnitudes in the TL and ME simulations that exhibit self-aggregation. However, the details of those two experiments are different. In TL, the contributions from longwave radiation are several times larger than those from shortwave radiation. In ME, longwave radiation dominates before day 50, after which shortwave radiation contributes more and remains positive even when longwave contributions oscillate between opposite signs after day 75. The sign of the radiative contribution depends on whether clouds produce relative heating (positive) or cooling (negative) in moist regions.

The advective contribution depends on whether circulation causes the convergence of MSE into moist or dry columns. It exhibits significant high-frequency variability. After filtering out sub-daily signals, the advective contributions are always negative in ML and TE. In TL and ME experiments, advection suppresses the growth of column MSE variance at the beginning and supports it throughout the intermediate stages; in later stages, the advection term oscillates between positive and negative signs but is negative on average.

Overall, we found that, in self-aggregated simulations, radiative processes promote convection self-aggregation, although the partitioning between shortwave and longwave contributions varies. Surface enthalpy flux played a significant role in the ME run prior to day 35, but otherwise opposed convection clustering in ME and TL. Advection promoted convection self-aggregation throughout the intermediate stages, and notably, the positive contributions started at approximately the same time as surface enthalpy flux contributions became negative. For ML and TE, it seems plausible to consider that self-aggregation did not occur as the radiative and surface flux forcings were not strong enough. However, it seems also reasonable that no self-aggregation resulted from the opposing effect of the advection term.

3.3 Linear Stability Analysis

To evaluate the fundamental causes of self-aggregation, we considered linear stability analysis. Because $H' = H_* r'$, Equation (10) can also be written as follows with the CRH anomaly r' as prognostic variable:

$$\frac{\partial r'}{\partial t} = (\beta_S + \beta_R) r' + \nu \nabla^2 r', \tag{12}$$

This is a reaction-diffusion equation and allows us to conduct linear stability analysis if we assume that the coefficients are constant.

Figure 3A-D, E-H, and I-L shows how radiative heating, surface enthalpy flux, and advective contribution anomalies, respectively, depend on column MSE anomaly between days 10 and 30 in the simulations. The predominant feature in these plots is the complexity of the relations between the represented variables. For the fixed values of MSE anomalies (or the Laplacian of anomalies), various terms exhibit notable amplitudes of variability. For example, when the column MSE anomaly is zero, the radiative heating anomaly can vary between -20 and $20\,\mathrm{W\,m^{-2}}$, with an approximately homogeneous probability distribution between -10 and $10\,\mathrm{W\,m^{-2}}$. These results reflect the randomness of the relationship between convection and column MSE.

Nonetheless, we can still compute the expectation of the forcing terms for each bin of column MSE anomalies (or their Laplacian) based on their probability distribution functions (PDFs), which are presented as the black lines in Fig. 3A-L. In general, this shows that radiation anomalies are more sensitive than surface enthalpy flux anomalies, with the exception of the ME simulation, where surface flux sensitivity is smaller but nonetheless comparable to radiative heating anomalies. The

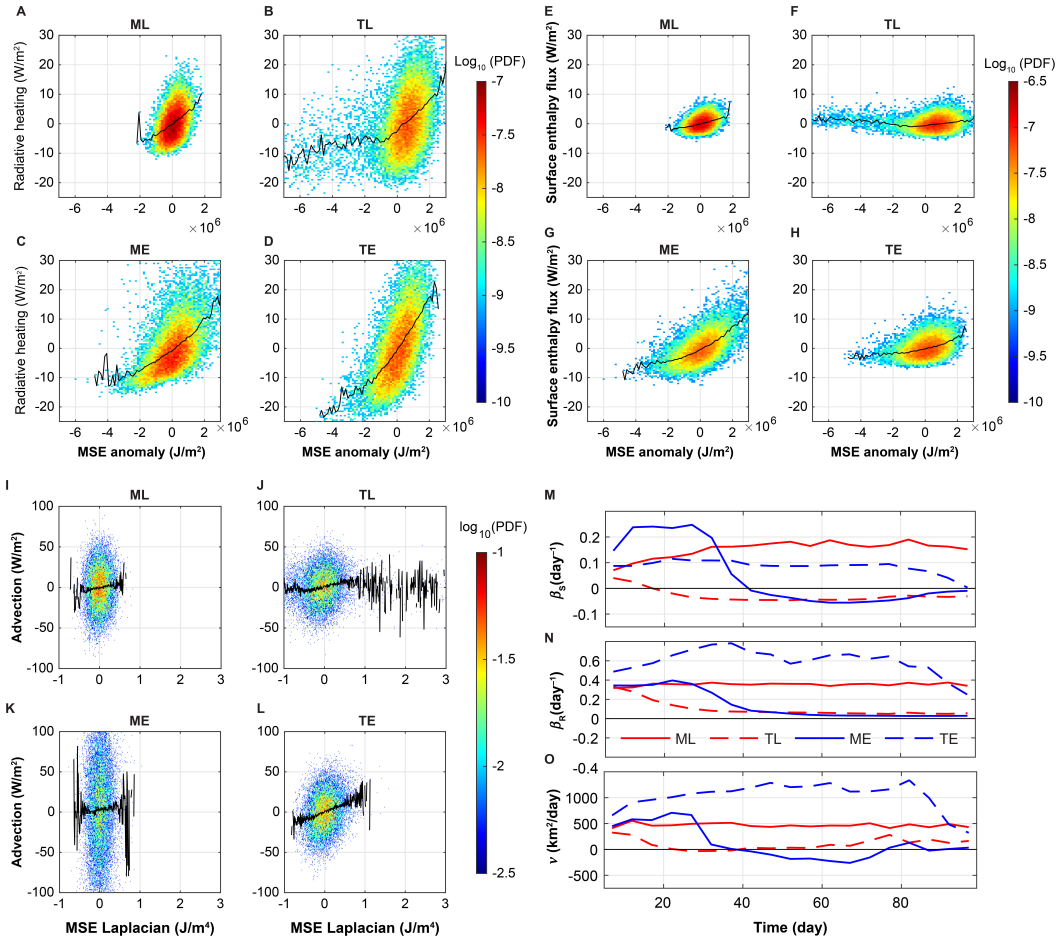

Figure 3. Feedback and circulation strengths for the linearized governing equation. Dependence of the radiative forcing anomaly (**A-D**), the surface enthalpy flux anomaly (**E-H**), and the advection anomaly (**I-L**) on the Laplacian of MSE anomalies between day 10 and 30 of the simulations. (**M-O**) Regressed coefficients based on 5-day periods.

sensitivities of radiative heating and surface enthalpy flux are mostly positive, such that radiation and surface flux correlate with cloudiness and gustiness, respectively, and tend to make moist (high MSE) columns more moist and dry columns drier. However, exceptions are observed in very dry (low MSE) columns, where the sensitivity may become negative. In ML and ME, radiative heating tends to increase as column MSE decreases near the left end of the diagrams, probably due to the spread of cirrus clouds into the dry regions. In TL, which exhibits a significant fraction of dry regions, surface enthalpy fluxes exhibit weak negative correlations with column MSE for dry columns, probably indicating the effect of the relative humidity of air on evaporation. Advection contributions exhibit mostly positive correlations with the Laplacian of column MSE, implying that advection tends to "diffuse" MSE from moist regions to dry regions, suppressing the development of separation between moist and dry columns. However, an interesting result presented in Fig. 3I-L is that eddy diffusivity can become negative for anomalously dry regions. Dry (low MSE) anomalies generally correspond to higher values of the Laplacian of column MSE. Thus, the right-hand side parts of Fig. 3J and K suggest that the values of effective eddy diffusivity are highly uncertain in dry regions and negative on average.

Despite the involved complexities, if we assume that the coefficients in Equation (12) are spatially uniform values that slowly change with time, we can regress the forcing terms onto the column MSE anomalies or their Laplacian and estimate the linear stability of Equation (12). The results of this regression are presented in Fig. 3M-O.

For cases in which the coefficients in Equation (12) are assumed to be constant, their solutions are the linear superposition of normal modes. By substituting the wave solution

$$r' = A_{kl} \exp(\mathrm{i}kx + \mathrm{i}ly + \sigma t) \tag{13}$$

into Equation (12), it can be found that the growth rate of the normal mode is

$$\sigma = (\beta_S + \beta_R) - \nu(k^2 + l^2) \tag{14}$$

This implies that the mode is unstable when the sum of terms in the first pair of brackets is larger than the last term. Equation (14) indicates that there is a critical wavenumber,

$$k_c = \sqrt{\frac{\beta_S + \beta_R}{\nu}} \tag{15}$$

above which the corresponding mode becomes stable. This criterion means that perturbation is needed to have a sufficient spatial scale (low wavenumber); otherwise, diffusion is too strong to allow perturbation to grow.

Figure 3M-O presents the regression coefficients for each 5-day period. This demonstrates that at the beginning of the simulations, coefficient values suggest that the critical wavelength is $\sim 70\Delta x$, where $\Delta x = 3\,\mathrm{km}$ is the horizontal grid spacing in the simulations. This wavelength is smaller than the domain size, $360\Delta x$, such that all simulations can potentially become unstable if large-scale perturbations occur. Indeed, although the ML and TE experiments did not develop self-aggregation during the 100 days of simulation tested, TE eventually exhibited aggregation behavior when the time between days 100 and 150 was integrated. We also verified that seeding a quadrant of the ML domain with a 30% water vapor deficit relative to its initial condition causes the dry area to grow and increase to 4/3 of the domain within 50 days.

Figure 3M-O demonstrates that TL and ME are destabilized by decreases in the effective diffusivity of the flow. In both simulations, the regression value of ν decreases with time, which is becoming close to zero or even negative. With such small diffusivity values, the critical wavenumber becomes very large, which means that small-scale perturbations can also be unstable and grow over time.

Physically, negative diffusivity corresponds to the formation of dry patches in the simulation domain. When dry patches form, the cloudiness of the corresponding regions is significantly reduced; thus, the radiative feedback is also weakened (Fig. 3B), causing parameter β_R to become small but still positive. Parameter β_S, which is related to surface flux, becomes negative as dry patches form due to the dependence of surface flux on moisture deficits (Fig. 3N). During the later stages of simulations, β_R and β_S become significantly smaller in the TL and ME runs, which exhibit self-aggregation, than in the ML and TE runs, which do not. Thus, we cannot argue that ML and TE did not exhibit self-aggregation as their radiative and surface flux feedbacks are not sufficiently strong. Instead, we suggest that their eddy diffusivity did not fall to values small enough to destabilize small-scale perturbations.

4 Bifurcation and Physical Parameterizations

4.1 Bifurcation in a Heuristic Model

Since Equation (13) is an eigenfunction of the Laplacian operator, we can heuristically express the diffusion term as a linear function of r' as follows:

$$\frac{dr'}{dt} = (\beta_S + \beta_R)r' + \nu k_0^2 r', \tag{16}$$

where k_0 denotes the characteristic wavenumber of the flow. In this ODE, assuming that the coefficients in brackets are constant, we conclude only that the stability of the system changes when the ratio of coefficients crosses one. However, from the above analysis, we know that the RCE is in a metastable state without self-aggregation. In Fig. 3M-O, we observe that when air columns become significantly dry or moist, β_R and β_S become smaller or even negative. Such radiative and surface flux feedbacks can be qualitatively represented by parameterizing the coefficients as a nonlinear function of CRH as follows:

$$\beta_S + \beta_R = C(0.81\tilde{r}^2 - \tilde{r}^4), \tag{17}$$

where C is a constant and $\tilde{r}$ is a scaled CRH perturbation that falls between approximately -1 and 1.

Substituting this expression into Equation (16) yields

$$\frac{d\tilde{r}}{dt} = (0.81\tilde{r}^2 - \tilde{r}^4)\tilde{r} + \alpha\tilde{r}, \tag{18}$$

in which the constant C and scaling factor related to $\tilde{r}$ are absorbed into the definition of time and $\alpha = \nu k_0^2 C^{-1}$. In this heuristic model, the radiative and surface flux forcing terms are infinitesimal when the perturbation is small, reflecting the effect of the randomness of cloudiness and gustiness (Fig. 3A-H). They exhibit positive (negative) forcings as CRH increases (decreases); however, when the CRH anomaly becomes too large (small), the forcing weakens (strengthens) (see black curve in Fig. 4A). The decreasing (increasing) trend of the forcing term at extremely high (low) values of $\tilde{r}$

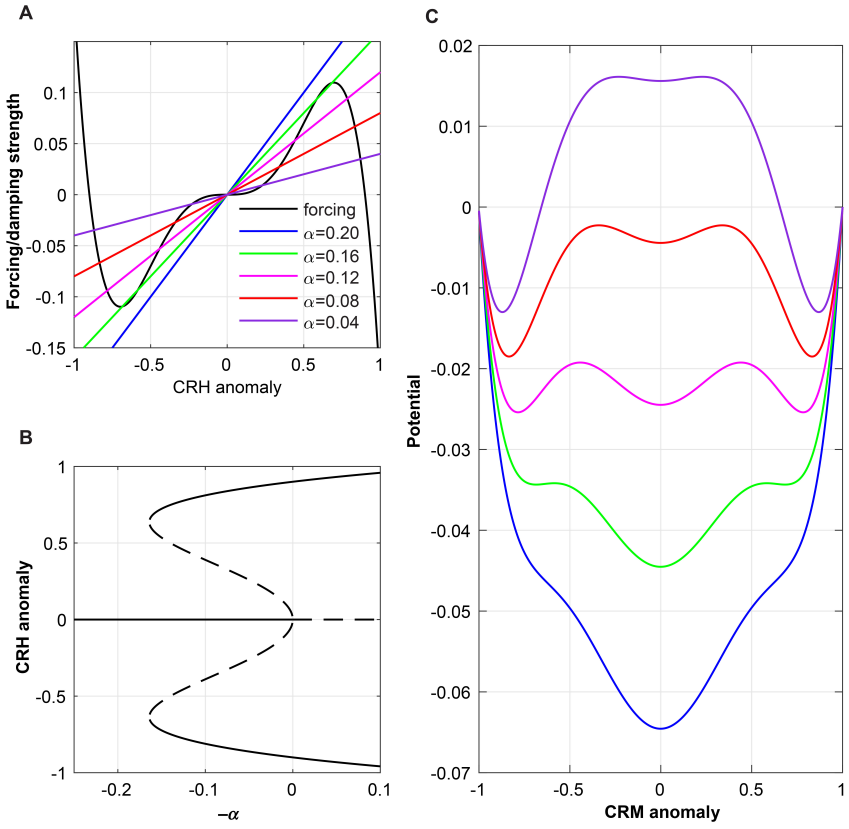

Figure 4. Bifurcation in the heuristic model. (**A**) Shape and amplitude of the radiative and surface flux forcing term (black curve) and the damping term (colored straight lines). (**B**) Fixed points of the model as a function of $-\alpha$; solid lines indicate stable fixed points, and dashed lines indicate unstable fixed points. (**C**) The potential function V in the model as a function of $-\alpha$.

reflects the fact that other physical constraints in nature prevent a column from approaching 100% (0%) CRH, which may actually rely on a change in the damping coefficient α in extreme conditions. Here, we parameterize this effect in the forcing term for convenience. Such a simplification does not qualitatively change the explanation of bifurcation behavior detailed below.

In Equation (18), α denotes the governing parameter, the inverse of which can be interpreted as a damping time scale. As presented in Fig. 4, when α is large, the amplitude of the damping term is larger than the forcing term for any CRH perturbation. When α becomes smaller, four fixed points ($d\tilde{r}/dt = 0$) other than the origin emerge in the diagram. When α is positive, the origin and the two fixed points with larger amplitudes are stable fixed points; thus, they attract states surrounding them in the phase space. The other two fixed points, i.e., those with smaller amplitudes, are unstable. When α crosses 0, the origin becomes unstable, the fixed points with larger amplitudes remain, and the unstable fixed points with smaller nonzero amplitudes disappear. In this situation, the RCE state with a uniform distribution of CRH is destabilized, and the system develops either a positive or negative large-amplitude CRH anomaly. The point at $\alpha = 0$ therefore corresponds to a subcritical bifurcation, across which the stability of the system dramatically changes.

We can derive a potential V for the right side of Equation (18) to gain further insight as follows:

$$\frac{d\tilde{r}}{dt} = -\frac{dV}{d\tilde{r}}\,. \tag{19}$$

The shape of the potential function (Fig. 4C) helps us appreciate the nature of this bifurcation. When the damping coefficient α is large, only one potential well exists at the zero CRH anomaly. As the damping weakens, two additional potential wells form at nonzero CRH anomaly values. However, those two wells are initially shallower than that at the origin; thus, the system still favors the zero CRH anomaly state when random perturbations exist. Eventually, when the damping becomes very weak, the potential well at the origin enters a metastable state, whereas the other two wells with nonzero CRH anomaly become the most stable, such that the system favors self-aggregation. When the damping coefficient α becomes negative, the potential well at the origin disappears.

The idea that convective self-aggregation corresponds to bifurcation was first proposed by Emanuel et al. (2014). However, they proposed that the SST was the governing parameter of the dynamical system. Here, focusing on the effects of physical parameterization schemes on simulations, our governing parameter is α, which describes the ratio of damping sensitivity to that of radiative and surface flux forcings. Although this heuristic model is simple, it approximates the behavior of numerical simulations. The initial critical wavelengths are smaller than the domain size, indicating the existence of metastable potential wells that correspond to self-aggregated states. Without large-scale perturbations in the initial conditions, the state with the lowest potential has a uniform distribution of convection and moisture. Later, between days 20 and 30, TL and ME simulations develop near-zero or negative diffusivity, causing bifurcation to occur. The uniformly distributed convection then enters an unstable state, and self-aggregation occurs.

4.2 Dry Plumes and Self-Aggregation

From the analysis above, we argue that the reduction of effective flow diffusivity to near-zero or negative values marks a bifurcation point across which self-aggregated states become more stable. In this section, we investigate the physical process causing near-zero or negative diffusivity.

As documented by previous studies (Bretherton et al., 2005; C. J. Muller & Held, 2012; C. Muller & Bony, 2015; B. Yang & Tan, 2020), the shallow circulation surrounding a dry patch exports moist low-level air out of the dry columns and imports relatively dry air from the middle and upper atmospheres. Thus, the formation of a dry patch is responsible for small or even negative diffusivity in the flow. Figure 5B–C presents the mesoscale circulation (arrows) on the cross sections of a growing dry patch. In three-dimensional space, it appears to be more appropriate to term the regions with low MSE "dry plumes," since the bulk of the negative MSE anomaly extends from the top of the boundary layer to the mid-troposphere. Circulation in and around these dry plumes features low-level divergence and upper-level convergence. The near-surface outflow air is dry relative to

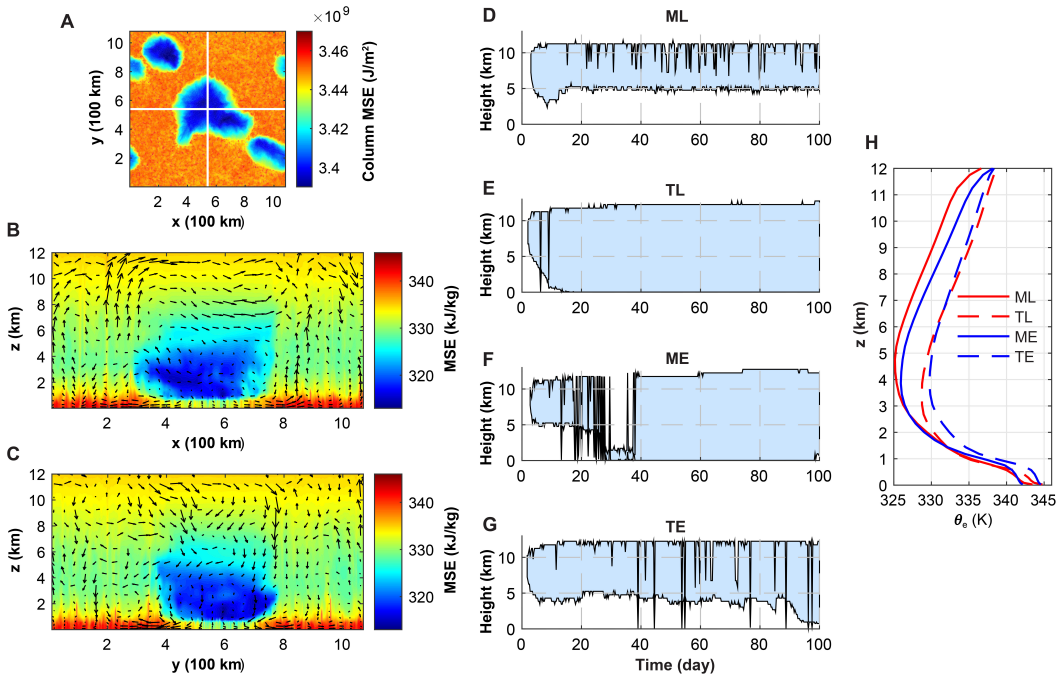

Figure 5. Dry plume dynamics and evolution. (**A**) Vertically integrated MSE in the TL simulation at Day 50. (**B**) and (**C**) Cross sections at the same time across the dry patch indicated with white lines in (**A**). Color shading indicates MSE (10^3 J/kg), and arrows indicate mesoscale wind fields. (**D–G**) Depths of the deepest dry plumes in the four simulations as functions of time. Light-blue shading indicates the bottom and top of the dry plume with the lowest bottom height at a given time. One dry plume is defined as a connected region in which the water vapor mixing ratio is less than 70% of the horizontal mean. (**H**) Mean profiles of equivalent potential temperature (θ_e) between days 40 and 60 of the simulations.

near-surface air away from the dry plumes. However, by virtue of enhanced surface latent heat flux, when this air reaches the lateral boundaries of the dry plumes, its moisture content is very close to that of the air away from the dry region. In the upper levels, air flows into the dry columns. This inflow is not particularly dry compared with the horizontal mean of MSE. However, its MSE is lower than the outflow air in the boundary layer. Therefore, as described in previous studies, low-level circulation is primarily responsible for the divergence of MSE from the dry regions.

Figure 5D–G presents the maximum depths of dry plumes in all simulations. Dry plumes can easily form in the upper troposphere as the atmosphere is absolutely stable above 5 km (Fig. 5H). Thus, upper-level dry plumes extending from 5 to 11 km were found to exist throughout all simulations. The deepening of dry plumes in the TL simulation appeared to be smooth. However, in all other simulations, a significant resistance to the formation of low-level plumes was observed. In the ML simulation, the dry plume did not reach the ground. In the TE simulation, dry plumes reached the ground several times, but these plumes were short-lived and rapidly retracted to the upper troposphere. Stable deep dry plumes did not form in the TE simulation until after day 95.

The formation of deep dry plumes in the ME simulation appears to differ from that in the ML simulation. Upper troposphere dry plumes formed in the ME simulation after approximately day 3. Although deepening occurred a few times, it was not successful. Eventually, between days 25 and 38, dry plumes reached the ground, but the plume was cut off from the middle and upper troposphere. Around day 40, deep dry plumes penetrating the troposphere formed in the ME simulation and advection began to support the growth of self-aggregation (Fig. 2E).

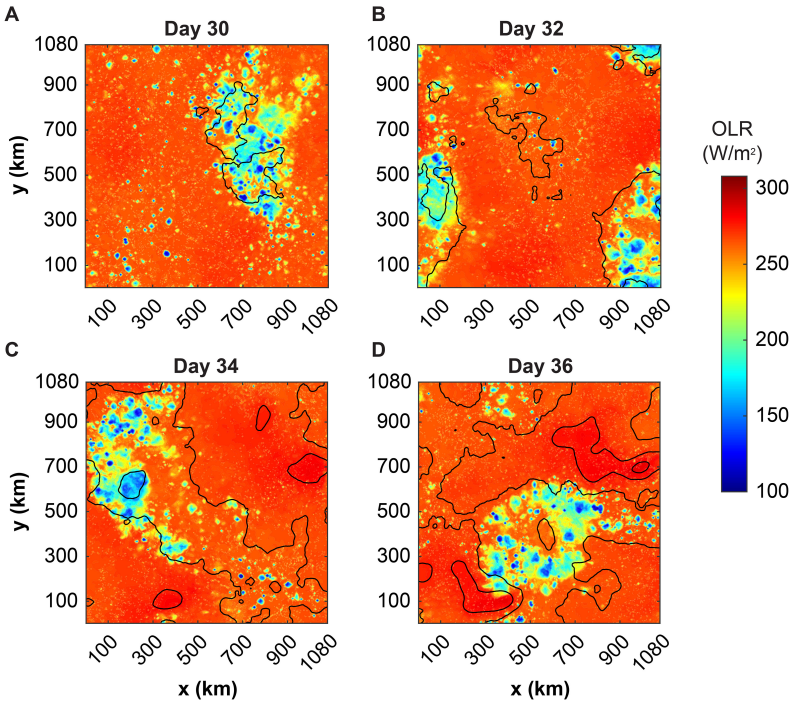

Figure 6. Clustering of convection without dry-moist patch separation in the ME simulation. Outgoing longwave radiation (OLR) (color shading) and column MSE distribution (contours) in the ME simulation between days 30 and 36. As in Fig. 1, contours are low-pass-filtered to reflect mesoscale patterns and are provided at intervals of $1 \times 10^7\,\mathrm{J\,m^{-2}}$.

Further examination of the results from the ME simulation between days 30 and 36 (Fig. 6) revealed that convective motions during this period formed a single cluster, although column MSE anomalies were still relatively weak. This suggests that, if self-aggregation is defined only as the clustering behavior of convection, instead of including the clear separation between dry and moist regions, it has already reached a peak by day 35 in the ME simulation. Figure 3M–O demonstrates that this early "aggregation" in the ME simulation may reflect interactions between convection, gustiness, and surface enthalpy flux.

Note that the definition of α in Equation (18) includes the coefficient C, which indicates the amplitude of the radiative and surface flux forcing terms. Destabilization can occur in two ways, either by enhancing the radiation and surface flux forcing terms or by reducing the effective diffusivity. Strictly speaking, the first approach is not a bifurcation as it decreases α but cannot directly produce negative α values. However, since perturbations in the simulation are of finite amplitudes instead of being infinitesimal, it is likely that the surface enthalpy flux feedback in the ME simulation caused the uniform state potential well to become shallower and decreased the potential of nonuniform states, resulting in the emergence of a dry plume with of finite-amplitude perturbations and thus negative diffusivity.

4.3 Cloud Microphysics

In this section, we investigate the role played by cloud microphysics parameterizations in bifurcation modulation. Figure 3A–D provides some clues. An important difference between the simulations using the Morrison microphysics scheme (ML and ME) and those using the Thompson scheme (TL and TE) is that a negative correlation develops at low MSE anomaly values for the period presented in Fig. 3. This local negative correlation between radiative heating and the MSE anomaly

indicates that dry, cold areas tend to be covered by high cirrus clouds, which leads to lower radiative cooling and favors convection.

Figure 7 presents the mean profiles of cloud water, cloud ice, rain, and snow (including graupel) mixing ratios between days 10 and 30 in the simulations. Figure 7A and B presents the mean profiles when the entire domains are included. The Morrison scheme experiments (ML and ME) consistently predict more cirrus clouds near the tropopause, whereas the Thompson scheme experiments (TL and TE) predict more snow. Figure 7C and D presents the mean profiles when only the driest mesoscale blocks in each time slice are included. The ML simulation still exhibits a significantly larger amount of cloud ice compared with others.

All cloud and precipitation species can affect the radiation budget of the atmosphere. However, due their smaller sizes, cloud ice particles are more efficient in altering radiative fluxes compared with snow. Figure 7E and F presents the relationships between column integrated ice and snow mass and corresponding OLR in ML and TL simulations. Those two panels do not demonstrate the same distributions and relationships, possibly due to their differing predictions of liquid water below the ice and snow. Nonetheless, Fig. 7E and F demonstrates that small amounts of change in cloud ice mass can cause large changes in OLR; if caused by snow mass variability, a change in snow mass of one order of magnitude is required.

Therefore, the critical difference between the Morrison and Thompson schemes is their prediction of cloud ice, which is influenced by how they partition condensate between cloud ice and snow, among other species. The Morrison scheme tends to produce more cirrus clouds, which results in a radiative heating anomaly that triggers convection. When cirrus clouds extend to dry blocks, their

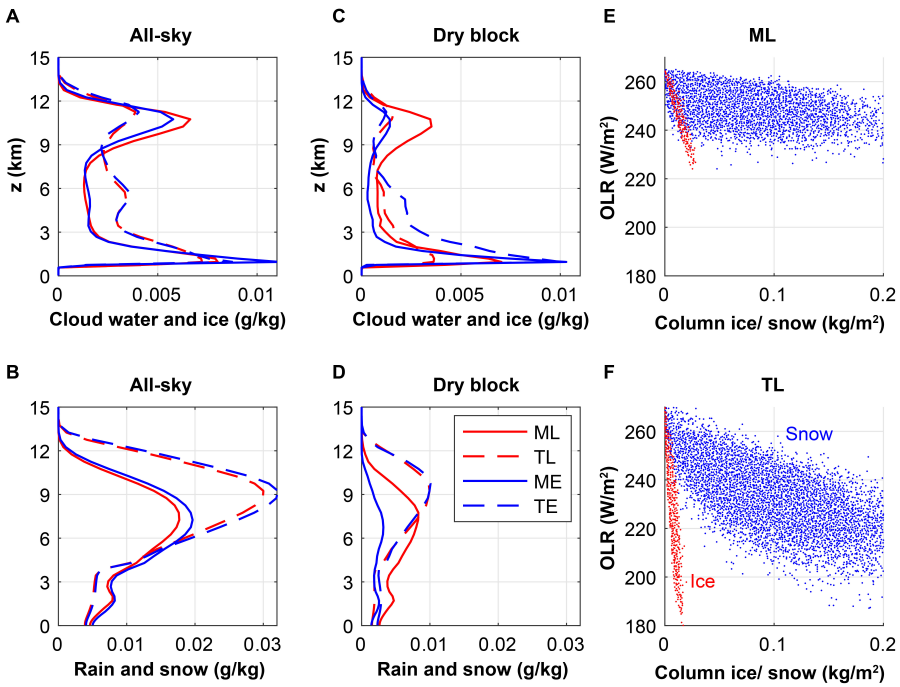

Figure 7. Cloud and precipitation profiles and radiative effect. (**A**) and (**C**) Mean profiles of the mixing ratios of cloud water and ice. (**B**) and (**D**) Rain and snow (including graupel) in all-domain averaged blocks (**A**) and (**B**) and in only the driest mesoscale blocks (**C**) and (**D**). (**E**) and (**F**) Relationship between OLR and column integrated ice and snow (including graupel) from the entire domains. Data between day 10 and day 30 of the simulations are used for all panels.

radiative effects prevent the formation of dry plumes. Thus, in Fig. 5D, dry plumes form in the stable upper troposphere but never extend downward to the conditionally unstable lower troposphere.

Why did the ME simulation lead to the formation of dry patches? From Fig. 7C, we can observe that the cirrus clouds in the ME run did not significantly intrude dry blocks. As argued in the previous section, the formation of dry patches in the ME appears to result from the interactions among convection, gustiness, and surface enthalpy fluxes. It is likely that the relative radiative heating in the ME simulation developed a coupling with surface enthalpy flux, and together, these phenomena caused the development of very intense convection cells in the ME. As a result, the downdraft in the dry region in ME is also stronger than that in other simulations and was sufficient to dissipate the cirrus cloud cover.

4.4 Turbulence Parameterization

The parameterization of turbulence in the planetary boundary layer (PBL) also played a significant role in bifurcation modulation in the RCE. As presented in Fig. 5H, the lower troposphere in the RCE is conditionally unstable. Once triggered, moist convection can bring moist, warm air upward, and tend to destroy dry plumes. It should be noted that Fig. 5H presents data between days 40 and 60 of the simulations, during which dry patches had already formed in the TL and ME simulations. In other words, the formation of dry patches does not alter the conditional unstable stratification in the lower troposphere of the RCE. Instead, their formation merely suppresses the triggering of moist convection.

Figure 8A–D demonstrates this relationship between the lower troposphere static stability and dry patch formation. $\Delta\theta_e$ in Fig. 8 denotes changes in equivalent potential temperature from 1 to 4 km above the surface in each column of the simulation domains. In simulations without dry patch formation (ML and TE), most columns have $\Delta\theta_e$ close to -10 K, indicating that the lower troposphere is conditionally unstable. Under certain rare conditions, the lower troposphere becomes moist neutral ($\Delta\theta_e = 0$). Such columns correspond to areas of intense convection. In the ME and TL simulations, the distributions of $\Delta\theta_e$ develop into bimodal ones as dry patches form. Dry patches correspond to the mode centered around -20 K, and regions with clustered convection form another mode, which is close to moist neutral due to convection-driven vertical mixing.

The difference between the Louis-type and EDMF turbulence schemes is implied by the upper and lower boundaries of the PDFs in Fig. 8B and C. In the TL simulation, the minimum $\Delta\theta_e$ reaches -30 K during the later stage of the run, whereas the maximum rarely exceeds 0 K. Contrarily, $\Delta\theta_e$ in the ME simulation is larger than -20 K for most of the simulation and reaches -25 K only by the end of day 100. The maximum $\Delta\theta_e$ in the ME simulation exhibits significant probability for values larger than 0 K. These differences indicate that the EDMF scheme favors the triggering of more intense and frequent convection than the Louis-type scheme.

The essential difference between the Louis-type and EDMF schemes is that the EDMF scheme can represent counter-gradient (i.e., nonlocal) vertical mixing instead of being restricted by local down-gradient transport. Moreover, EDMF can extend its effects above the capping inversion of the PBL. Thus, these two PBL schemes have significantly different capabilities for triggering convection in the conditionally unstable lower troposphere. Figure 8E–H presents the joint PDFs of turbulence tendency due to PBL schemes and vertically integrated moisture anomalies between 0.5 and 1.5 km above surface. Both with and without the formation of dry patches, the tendency due to the Louis-type scheme is very close to zero in this layer, which lies immediately above the boundary layer. Contrarily, the EDMF scheme tends toward significant moistening. The EDMF scheme is also more sensitive to moisture variability in this layer, such that its tendency increases (decreases) significantly when the layer dries (moistens).

In summary, the TE experiment was demonstrated to be very slow in developing dry patches due to the effects of convection triggering in the EDMF scheme. For the same reason, when dry patches form in the TL and ME simulations, the latter has a relatively more stable lower troposphere than the former (Fig. 8B and C). Although the ML simulation does not exhibit significant moistening

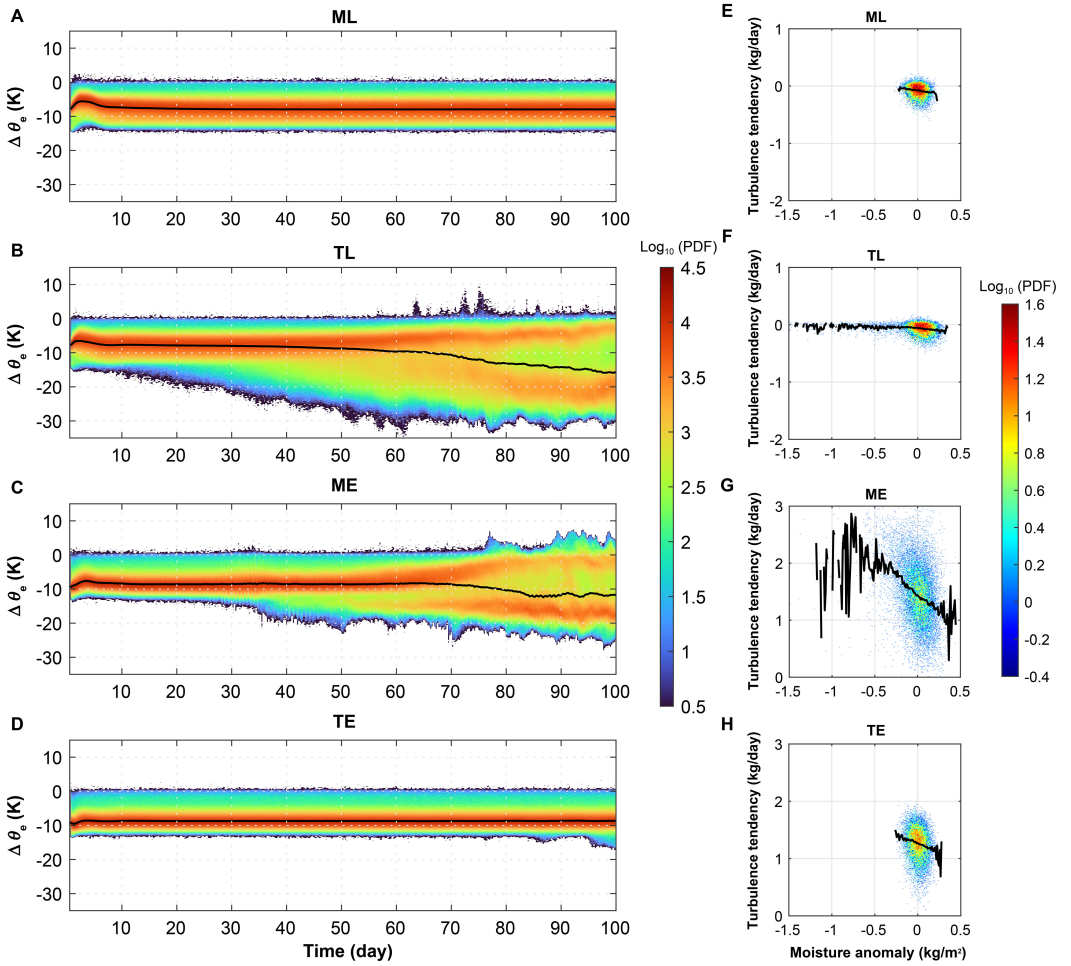

Figure 8. Lower troposphere stability and PBL turbulence tendency. (**A-D**) Logarithm of PDFs of change in equivalent potential temperature (θ_e) from 1 to 4 km above the surface in mesoscale blocks. Black lines indicate the horizontal mean $\Delta\theta_e$ at a given time. Panels (**E-H**) show the time tendency of mesoscale block moisture integrated between 0.5 and 1.5 km above the surface in the PBL turbulence schemes for days 10 to 30. Black lines indicate the mean tendency for each bin of moisture anomaly.

and destabilization due to the PBL scheme, as discussed above, it did not form dry patches as a result of column heating anomalies related to cirrus clouds over dry blocks.

5 Summary and Discussion

Through a matrix of numerical experiments employing two cloud microphysics schemes and two boundary layer turbulence schemes, we demonstrated that the emergence of self-aggregation in the RCE is not simply tied to a certain kind of parameterization. Instead, self-aggregation, which is defined here as the formation and clear separation of dry and moist columns, is related to a bifurcation of the underlying dynamical system of the RCE.

In the linearized equation of vertically integrated MSE, the stability of the spatially uniform MSE state is governed by the strengths of radiative and surface enthalpy flux feedbacks as well as the effective eddy diffusivity of the flow. In all simulations, linear stability analysis suggests that sufficiently large-scale perturbations are unstable. However, without seeding large-scale perturbations

in the initial conditions, such phenomena may not occur spontaneously. Critical for destabilizing the uniform RCE state is the formation and maintenance of dry patches, which lead to the formation of shallow circulation and lower the effective horizontal eddy diffusivity to zero or even negative values. With near-zero eddy diffusivity, the RCE atmosphere can easily be destabilized by radiative and surface enthalpy feedbacks, even though their strengths weaken with the spatial expansion of dry patches.

By representing RCE dynamics with a heuristic ODE model, we demonstrated that self-aggregation in RCE corresponds to the bifurcation of the dynamical system. When feedback strengths are relatively weak and diffusion is relatively strong, the uniform state has the lowest potential. When diffusion weakens and dry patches form, anomalously moist states gain relatively lower potentials and can enter a more stable state. When eddy diffusion becomes negative (i.e., a counter-gradient), uniform moisture distribution becomes an unstable solution.

Thus, we show that bifurcation in the RCE is marked by the formation and maintenance of dry patches, which may be more accurately termed dry plumes as they correspond to a three-dimensional volume with anomalously low moisture. Different physical schemes can certainly alter feedback strengths and thereby accelerate or decelerate relevant processes. However, our analysis suggests that the role played by these schemes in creating or destroying dry plumes is more critical. Because the lower troposphere in the RCE is conditionally unstable, the formation of dry plumes depends on its capacity to suppress or trigger moist convection when dry plumes from the upper troposphere extend to touch the ground, irrespective of the physics scheme used. The Morrison scheme tends to produce more cirrus clouds, which introduce radiative heating anomalies over dry regions and trigger convection. This, in turn, destroys dry plumes (ML). However, when an abundance of cloud ice combines with an active turbulence scheme, their coupling can generate intense convection clusters, increasing downward flow and forcing the formation of a low-level dry plume (ME). The Thompson scheme does not produce excessive ice over dry blocks. Therefore, when paired with the less-active Louis PBL scheme, dry plumes form quite easily (TL). However, when paired with the EDMF scheme, which models the counter-gradient, PBL-penetrating turbulence fluxes, i.e., low-level dry plumes, were destroyed by the moist convection frequently triggered by the EDMF scheme (TE).

Our study increases the understanding of the complexity of physical parameterization in the gray zone of weather and climate models. The nonlinear characteristics of the dynamics of the tropical atmosphere enable the same kind of convection organization to be tuned via multiple pathways, i.e., through the modification of cloud microphysics, PBL turbulence, or both. The need to unify turbulence and cloud parameterization has been recognized in recent years (Bodenschatz et al., 2010; Bogenschutz & Krueger, 2013; Thayer-Calder et al., 2015). However, contrary to previous studies, which highlight the interaction of turbulence and cloud physics at the microscale, our study documents how these two processes can, either by themselves or by interaction, influence the macroscale organization of convection. In spite of the fact that they share the same prescribed SST, the RCE states of our four simulations (Fig. 1) exhibit drastically different intensities and distributions of albedo, OLR, precipitation, and evaporation. Thus, for both weather and climate prediction in the gray zone, the representation of microscale physical processes can modulate the simulation of large-scale phenomena in notable ways.

The numerical simulations presented here used idealized setups; therefore, it is unknown whether and how the bifurcation mechanism outlined here may interact with preexisting large-scale perturbations in the tropical atmosphere. It is possible that large-scale perturbations are dominant over microscale processes (Durran & Gingrich, 2014), such that microphysics and turbulence play a lesser role in influencing the large-scale characteristics of the simulated atmosphere. However, we consider it more likely as we have learned that turbulence and cloud processes have dramatic impacts on large-scale climate (Bretherton, 2015; Schneider et al., 2017, 2019).

Developing turbulence and cloud parameterizations for the gray zones are challenging tasks that we need to confront for advancing our weather and climate models further. The bifurcation mechanism discussed herein poses a possible fundamental barrier to our efforts to improve the representation of subgrid-scale processes. When large-scale circulation has a sensitive and discontinuous

dependence on subgrid-scale processes, nonlinearity in their relationship may render parameter tuning very difficult. Furthermore, some fundamental limits might exist on the uncertainties of microscale process parameters that cannot be narrowed down, for example, due to the randomness of turbulence. In this situation, deterministic parameterizations may possess some limitations in their predicting capabilities because the fixed choices of parameters might rule out some qualitatively different system states from a model's solutions. As the NWP community did for overcoming initial condition uncertainties, ensemble-based approaches, (e.g., Grell & Freitas, 2014), may also be necessary for physical parameterizations to mitigate the nonlinear effects.

We are familiar with using Lorenz's iconic phrase "the butterfly effect" to describe the sensitive and possibly discontinuous dependence on initial conditions, which sets potential limits to a system's predictability (Palmer et al., 2014). The nonlinear dependence on subgrid-scale process parameters in our discussion herein is another kind of the butterfly effect. This second kind of butterfly effect might represent fundamental barriers to the predictability of climate. We may never represent the exact physics of cloud and turbulence in climate models due to computational cost, or limitations of our knowledge, or both. Therefore, through bifurcation mechanisms, slight differences in the approximations adopted by different modelers may always cause significant differences in the predicted climates, at least for some processes.

Acknowledgments

We thank the Research Grants Council of Hong Kong SAR, China, University Grants Committee of Hong Kong for supporting the project (HKUST 26305720). The CM1 code was kindly provided by Dr. George Bryan and can be downloaded from https://www2.mmm.ucar.edu/people/bryan/cm1/. The namelist files used to run CM1 to produce the numerical experiments in this study can be found at https://github.com/shixm-cloud/rce-bifurcation.

References

Adams-Selin, R. D., van den Heever, S. C., & Johnson, R. H. (2013). Impact of graupel parameterization schemes on idealized bow echo simulations. *Mon. Wea. Rev.*, *141*(4), 1241–1262.

Benjamin, S. G., Weygandt, S. S., Brown, J. M., Hu, M., Alexander, C. R., Smirnova, T. G., ... others (2016). A north american hourly assimilation and model forecast cycle: The rapid refresh. *Mon. Wea. Rev.*, *144*(4), 1669–1694.

Beucler, T., & Cronin, T. W. (2016). Moisture-radiative cooling instability. *J. Adv. Model. Earth Syst.*, *8*(4), 1620–1640.

Bodenschatz, E., Malinowski, S. P., Shaw, R. A., & Stratmann, F. (2010). Can we understand clouds without turbulence? *Science*, *327*(5968), 970–971.

Bogenschutz, P. A., & Krueger, S. K. (2013). A simplified pdf parameterization of subgrid-scale clouds and turbulence for cloud-resolving models. *J. Adv. Model. Earth Syst.*, *5*(2), 195–211.

Bretherton, C. S. (2015). Insights into low-latitude cloud feedbacks from high-resolution models. *Phil. Trans. R. Soc. A*, *373*(2054), 20140415.

Bretherton, C. S., Blossey, P. N., & Khairoutdinov, M. (2005). An energy-balance analysis of deep convective self-aggregation above uniform sst. *J. Atmos. Sci.*, *62*(12), 4273–4292.

Bryan, G. H., & Fritsch, J. M. (2002). A benchmark simulation for moist nonhydrostatic numerical models. *Mon. Wea. Rev.*, *130*(12), 2917–2928.

Bryan, G. H., & Morrison, H. (2012). Sensitivity of a simulated squall line to horizontal resolution and parameterization of microphysics. *Mon. Wea. Rev.*, *140*(1), 202–225.

Bryan, G. H., & Rotunno, R. (2009). The maximum intensity of tropical cyclones in axisymmetric numerical model simulations. *Mon. Wea. Rev.*, *137*(6), 1770–1789.

Chow, F. K., Schär, C., Ban, N., Lundquist, K. A., Schlemmer, L., & Shi, X. (2019). Crossing multiple gray zones in the transition from mesoscale to microscale simulation over complex terrain. *Atmosphere*, *10*(5), 274.

Durran, D. R., & Gingrich, M. (2014). Atmospheric predictability: Why butterflies are not of practical importance. *J. Atmos. Sci.*, *71*(7), 2476–2488.

Emanuel, K., Wing, A. A., & Vincent, E. M. (2014). Radiative-convective instability. *J. Adv. Model. Earth Syst.*, *6*(1), 75–90.

Grell, G. A., & Freitas, S. R. (2014). A scale and aerosol aware stochastic convective parameterization for weather and air quality modeling. *Atmos. Chem. Phys.*, *14*(10), 5233–5250.

Hong, S.-Y., & Pan, H.-L. (1996). Nonlocal boundary layer vertical diffusion in a medium-range forecast model. *Mon. Wea. Rev.*, *124*(10), 2322–2339.

Lean, H. W., Clark, P. A., Dixon, M., Roberts, N. M., Fitch, A., Forbes, R., & Halliwell, C. (2008). Characteristics of high-resolution versions of the met office unified model for forecasting convection over the united kingdom. *Mon. Wea. Rev.*, *136*(9), 3408–3424.

Manabe, S., & Strickler, R. F. (1964). Thermal equilibrium of the atmosphere with a convective adjustment. *J. Atmos. Sci.*, *21*(4), 361–385.

Milbrandt, J. A., Bélair, S., Faucher, M., Vallée, M., Carrera, M. L., & Glazer, A. (2016). The pan-canadian high resolution (2.5 km) deterministic prediction system. *Wea. Forecasting*, *31*(6), 1791–1816.

Morrison, H., Milbrandt, J., et al. (2011). Comparison of two-moment bulk microphysics schemes in idealized supercell thunderstorm simulations. *Mon. Wea. Rev.*, *139*(4), 1103.

Morrison, H., Thompson, G., & Tatarskii, V. (2009). Impact of cloud microphysics on the development of trailing stratiform precipitation in a simulated squall line: Comparison of one-and two-moment schemes. *Mon. Wea. Rev.*, *137*(3), 991–1007.

Morrison, H., van Lier-Walqui, M., Fridlind, A. M., Grabowski, W. W., Harrington, J. Y., Hoose, C., ... others (2020). Confronting the challenge of modeling cloud and precipitation microphysics. *J. Adv. Model. Earth Syst.*, *12*(8), e2019MS001689.

Muller, C., & Bony, S. (2015). What favors convective aggregation and why? *Geophys. Res. Lett.*, *42*(13), 5626–5634.

Muller, C. J., & Held, I. M. (2012). Detailed investigation of the self-aggregation of convection in cloud-resolving simulations. *J. Atmos. Sci.*, *69*(8), 2551–2565.

Palmer, T., Döring, A., & Seregin, G. (2014). The real butterfly effect. *Nonlinearity*, *27*(9), R123.

Raynaud, L., & Bouttier, F. (2017). The impact of horizontal resolution and ensemble size for convective-scale probabilistic forecasts. *Quart. J. Roy. Meteor. Soc.*, *143*(709), 3037–3047.

Romps, D. M. (2011). Response of tropical precipitation to global warming. *J. Atmos. Sci.*, *68*(1), 123–138.

Schneider, T., Kaul, C. M., & Pressel, K. G. (2019). Possible climate transitions from breakup of stratocumulus decks under greenhouse warming. *Nat. Geosci.*, *12*(3), 163–167.

Schneider, T., Teixeira, J., Bretherton, C. S., Brient, F., Pressel, K. G., Schär, C., & Siebesma, A. P. (2017). Climate goals and computing the future of clouds. *Nat. Clim. Change*, *7*(1), 3–5.

Seity, Y., Brousseau, P., Malardel, S., Hello, G., Bénard, P., Bouttier, F., ... Masson, V. (2011). The arome-france convective-scale operational model. *Mon. Wea. Rev.*, *139*(3), 976–991.

Thayer-Calder, K., Gettelman, A., Craig, C., Goldhaber, S., Bogenschutz, P. A., Chen, C.-C., ... others (2015). A unified parameterization of clouds and turbulence using clubb and subcolumns in the community atmosphere model. *Geosci. Model Dev.*, *8*(12), 3801–3821.

Thompson, G., Field, P. R., Rasmussen, R. M., & Hall, W. D. (2008). Explicit forecasts of winter precipitation using an improved bulk microphysics scheme. part ii: Implementation of a new snow parameterization. *Mon. Wea. Rev.*, *136*(12), 5095–5115.

Wedi, N. P., Polichtchouk, I., Dueben, P., Anantharaj, V. G., Bauer, P., Boussetta, S., ... others (2020). A baseline for global weather and climate simulations at 1 km resolution. *J. Adv. Model. Earth Syst.*, *12*(11), e2020MS002192.

Wing, A. A., Camargo, S. J., & Sobel, A. H. (2016). Role of radiative–convective feedbacks in spontaneous tropical cyclogenesis in idealized numerical simulations. *J. Atmos. Sci.*, *73*(7), 2633–2642.

Wing, A. A., Emanuel, K., Holloway, C. E., & Muller, C. (2018). Convective self-aggregation in numerical simulations: A review. In R. Pincus, D. Winker, S. Bony, & B. Stevens (Eds.), *Shallow clouds, water vapor, circulation, and climate sensitivity* (pp. 1–25). Cham: Springer International Publishing. doi: 10.1007/978-3-319-77273-8_1

Wing, A. A., & Emanuel, K. A. (2014). Physical mechanisms controlling self-aggregation of convection in idealized numerical modeling simulations. *J. Adv. Model. Earth Syst.*, *6*(1),

671 59–74.
672 Wyngaard, J. C. (2004). Toward numerical modeling in the "terra incognita". *J. Atmos. Sci.*, *61*(14),
673 1816–1826.
674 Yang, B., & Tan, Z.-M. (2020). The initiation of dry patches in cloud-resolving convective self-
675 aggregation simulations: Boundary layer dry-subsidence feedback. *J. Atmos. Sci.*, *77*(12),
676 4129–4141.
677 Yang, D. (2018). Boundary layer diabatic processes, the virtual effect, and convective self-
678 aggregation. *J. Adv. Model. Earth Syst.*, *10*(9), 2163–2176.
679 Yang, D. (2019). Convective heating leads to self-aggregation by generating available potential
680 energy. *Geophys. Res. Lett.*, *46*(17-18), 10687–10696.